International Journal of Non–Linear Mechanics 162 (2024) 104716

Contents lists available at ScienceDirect

International Journal of Non-Linear Mechanics

journal homepage: www.elsevier.com/locate/nlm

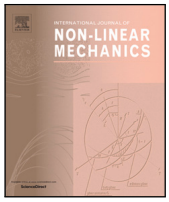

Propagation of compression solitary waves on tensegrity-like lattices made of truncated octahedrons

Julia de Castro Motta [a,*], Kevin Garanger [b], Julian J. Rimoli [b]

[a] Department of Civil Engineering, University of Salerno, Fisciano, 84084, Italy
[b] Department of Mechanical and Aerospace Engineering, University of California Irvine, Irvine 92697, USA

ARTICLE INFO

Keywords:
Tensegrity lattices
Initially soft response
Hardening
Solitary waves
Wave profile
Weierstrass theory

ABSTRACT

This work studies the properties of compression solitary waves propagating through one-dimensional mass–spring lattices, whose unit cells show an interaction law mimicking that of a truncated tensegrity octahedron. Analytic methods based on the Weierstrass criterion for compact solitary waves, and the long wave approximation theory are employed to demonstrate that the analyzed systems support compression solitary waves in a suitable range of wave speeds. These systems exhibit an initially soft response, which progressively turns into an elastically hardening behavior ending with a linear branch in the pre-buckling regime of the units cells. Explicit formulae are given for the lower and upper bounds of the wave speed interval that produce compact solitary waves, together with analytic laws of the shape of the traveling wave. Numerical simulations provide a validation of the presented theory.

1. Introduction

Tensegrity systems are lightweight structures formed by a continuous network of tensile members (cables) connected to compressive members (bars). The stiffness of these structures is strongly influenced by the presence of internal or external prestress, being therefore exceptionally tunable [1]. For these reasons, tensegrity structures have shown to be an interesting option in constructing metamaterials. Metamaterials can be defined as artificially structured lattices of unit cells exhibiting unconventional mechanical properties that are not necessarily present on the unit cell itself and are mainly due to their particular structural arrangement [2–5]. These properties can include, among others, the presence of frequency bandgaps, unusual responses to stresses and strains, and negative material properties. The use of tensegrity modules as metamaterials' units has led to interesting results such as the tunability of the frequency bandgaps, and the presence of localized solitary waves [6–12]. A special role is held by truncated octahedron tensegrity units [13,14], which have been tessellated into multi-dimensional lattices to form systems that exhibit a tunable propagation of linear and shear waves, via a change of prestress variables and by accounting for bar buckling [10]. A peculiar aspect of the geometry of a truncated octahedron is that it enables the tessellation of three-dimensional lattices, a feature with potential avenues in the field of mechanical metamaterials [13,15]. It is also possible to design truncated octahedron tensegrities such that they can be compressed to an almost flat state without any failure of their members, storing an important amount of energy in the meantime, which led to conceptual studies for using them as planetary landers [16,17].

This work studies the propagation of compression solitary waves in one-dimensional lattices formed by chains of truncated octahedron tensegrities loaded in compression, which are alternated with lumped masses. The attention is focused on the pre-buckling regime of the unit cell, which allows for the modeling a nonlinear elastic response of the system. The articulated nature of the force vs. displacement response in compression of a truncated octahedron [18] makes it impossible to obtain straightforward analytic results for the wave propagation response exhibited by the systems examined in the present work. The use of a 'tensegrity-like' potential, which retains the main features of the real potential of the unit cell, has proved to be a good option to perform such a study successfully, with reference to chains of tensegrity prisms [6]. The present paper extends this approach to mass–spring chains that employ truncated octahedron building blocks, whose force vs. displacement response has been shown to exhibit an initial soft-response, followed by a hardening branch that progressively turns into a linear branch, for increasing values of the axial displacement, before bars' buckling occurs [18]. The main difference between the mechanical behaviors of the truncated octahedron tensegrity and the tensegrity prism with rigid bases, studied in [6], lies in the fact that the tensegrity octahedron can be compressed until it reaches an almost flat configuration, while the tensegrity prism with rigid bases tends

* Corresponding author.
E-mail address: jdecastromotta@unisa.it (J. de Castro Motta).

https://doi.org/10.1016/j.ijnonlinmec.2024.104716
Received 30 December 2023; Received in revised form 10 March 2024; Accepted 25 March 2024
Available online 30 March 2024

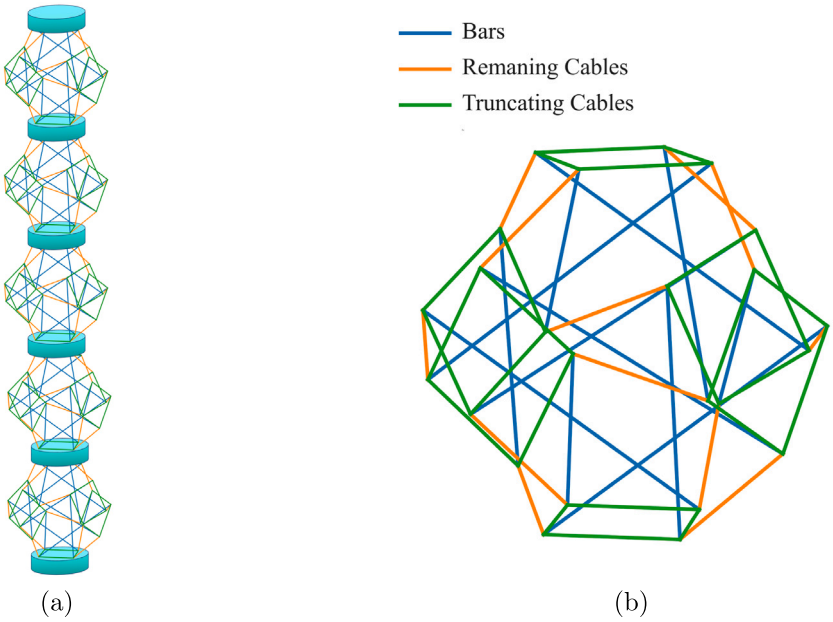

Fig. 1. One-dimensional chain (a) formed by lumped masses and truncated octahedron tensegrity units (b).

to achieve a locking configuration with tangent stiffness tending to infinity, as the bars start touching each other under increasing values of the compression displacement. However, both these systems exhibit an elastically hardening behavior, in appropriate displacement ranges, and therefore we expect that a chain of truncated octahedron tensegrities also supports the propagation of compression solitary waves, as the chains of tensegrity prisms studied in [6,7,19–21] .

The results presented in this study reveal that chains of tensegrity octahedrons support the propagation of compression solitary waves within a given range of wave speeds, that is, the existence of a minimum value (v_{min}) and a maximum value (v_{max}) of the wave speed that produce the formation of such pulses. Due to the tunability of the potential of the examined unit cells, we also show that it is possible to finely adjust the values of v_{min} and v_{max}, which proves to be useful for the design of novel acoustic materials with tunable wave-focusing capabilities [22–25]. The structure of the paper is as follows. Section 2 gives a brief description of the geometry, topology and mechanical response in compression of a truncated tensegrity octahedron. Section 3 presents a nonlinear tensegrity-like potential that is able to capture the main features of such a response. Section 4.1 analyzes the quasi-continuum limit of the equations of motion of the mass–spring chains under examination, when equipped with the tensegrity-like potential. The proof of existence of solitary waves in such systems, and their localization properties are discussed in Section 4.2. Section 5 illustrates numerical simulations that provide a validation of the theoretically predictions of Section 4. Finally, Section 6 presents concluding remarks and directions for future research.

2. Mechanical response in compression of an octahedron unit

Let us analyze the one dimensional chain of truncated octahedron tensegrity units alternated with lumped masses, which is shown in Fig. 1(a). The present section analyzes the mechanical response of the unit cell of this system, in presence of an uniaxial compression loading condition that is generated by a dynamic perturbation. We adopt a static approach to the constitutive equation of the unit cell, since we assume that the characteristic time of the wave propagation problem generated by the dynamic loading is significantly larger than the fundamental vibration period of the unit cell [20]. The cables of the structure are modeled as linear elastic springs that respond only in tension. As for the bars, they are also modeled as linear elastic springs, up to the displacement corresponding to their Euler's critical load, after which the force they generate is kept constant. The state of the structure is represented by the positions of the bars' ends, referred as nodes. Since there are 24 nodes in total, the unconstrained structure has 72 degrees of freedom. Within the present section, we numerically study the response of the unit cell up to the post-buckling regime of the bars, for completeness. The wave propagation problem analyzed in the following sections will instead be focused on the pre-buckling regime, as anticipated [14].

Starting from the stress-free configuration, the compression of the unit is simulated by imposing given vertical displacements to the four nodes of the top face, while the vertical displacements of the four nodes of the bottom face are constrained to zero. The horizontal displacements of both top and bottom nodes are unconstrained since we assume that the units are in frictionless contact with the lumped masses which free to move only along the vertical axis of the chain without rotating, thus not transmitting any bending or twisting moment (see [6] and references therein). The vertical displacements of the top nodes are assigned equal to each other into incremental steps. For each step, we let u denote the current value of such displacements (positive in compression), and we use the symbol F_{oct} to denote the magnitude of the overall compression forces acting on the top and bottom bases The incremental equilibrium problem of the unit cell is here briefly summarized.

Let h_0 be the height of the undeformed tensegrity unit cell at equilibrium. The quasi-static response of the unit cell in compression is determined by varying u from 0 to ϵh_0 in fixed increments, where $0 < \epsilon < 1$ is set such that buckling of the bars is reached, and by finding an equilibrium configuration of the unit cell at each step. Once the equilibrium position for a prescribed u is found, F_{oct} is set to the sum of the vertical forces at the nodes of the top face.

The equilibrium configuration of the structure at each step is found by solving the above incremental problem through a conjugate gradient descent method with a line search and a Polak–Ribière update rule [26].

At the start of each new loading step, a preconditioning phase of the displacements of the unconstrained nodes is performed, through the following procedure. If an unconstrained node achieves a given vertical displacement v at equilibrium under the global constraint $u = u_1$, we initialize its vertical displacement to $v \times (u_2/u_1)$ in correspondence to the next loading step, assuming that the global displacement constraint has

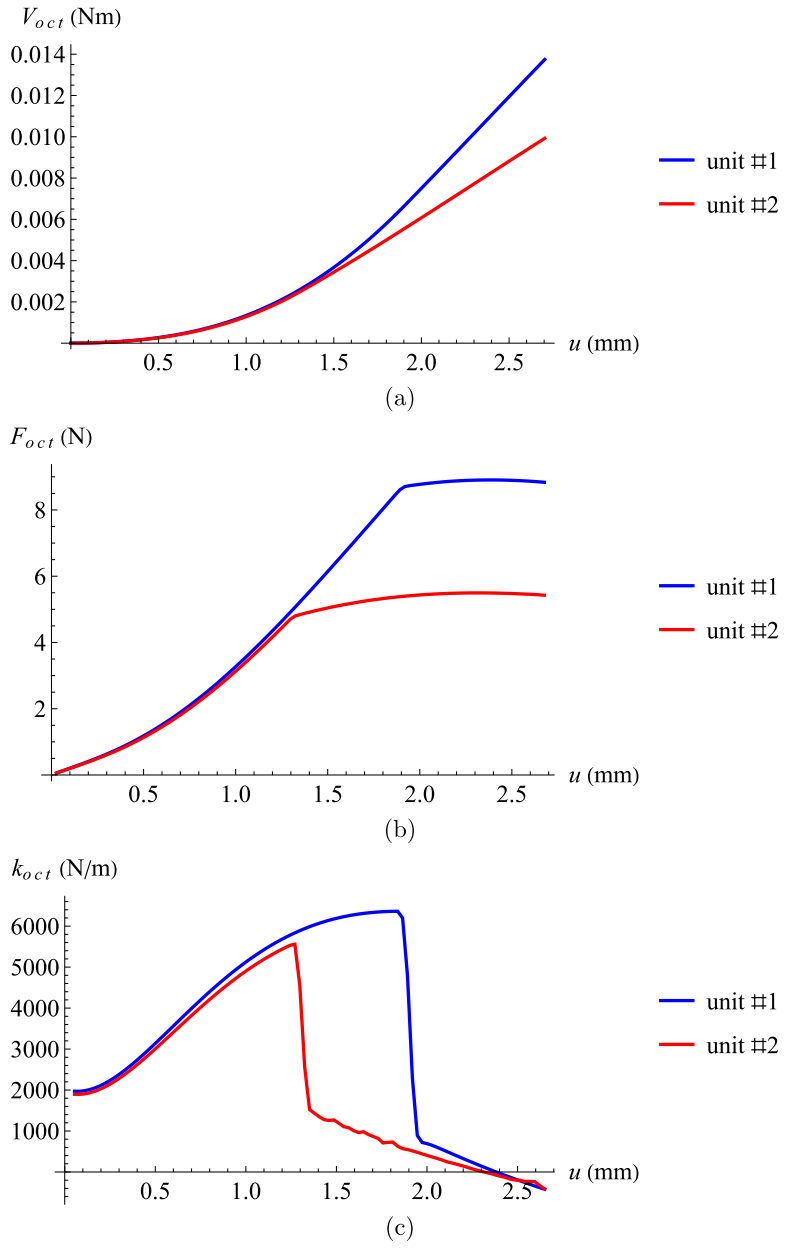

Fig. 2. V_{oct} vs. u (a) F_{oct} vs. u (b) and k_{oct} vs. u (c) responses of truncated octahedrons equipped with the properties listed in Table 1. The blue curves are exhibited by a truncated octahedron with circular bars showing diameter $d_{bar} = 0.03078$ mm (unit # 1), while the red curves pertain to a unit with $d_{bar} = 0.02676$ mm (unit # 2). (For interpretation of the references to color in this figure legend, the reader is referred to the web version of this article.)

been changed to $u = u_2$. While this preconditioning phase is not strictly necessary, it was numerically observed that it leads to a significant reduction of the convergence time.

To account for the buckling of the bar, the force resulting from a change in their length is modeled with a piecewise linear function, defined in (1). Given the bars' length at rest l_0, cross-section radius r, and Young's modulus E, the compressive force resulting from a deformed length l is given by

$$f_{\text{bar}}(l) := \begin{cases} \kappa(l_0 - l) & \text{if } l > l_{\text{cr}} \\ P_{\text{cr}} & \text{if } l \le l_{\text{cr}} \end{cases}, \tag{1}$$

where $\kappa := \frac{E\pi r^2}{l_0}$ is the pre-buckling stiffness of the bars, $P_{\text{cr}} := \frac{\pi^3 E r^4}{4 l_0^2}$ their Euler's critical load, and $l_{\text{cr}} := l_0 - \frac{P_{\text{cr}}}{\kappa}$ their length at buckling. The adoption of the Euler buckling theory, which assumes the inextensibility of compressed members, is justified by the fact that the initial length of the bars l_0 is rather close to l_{cr}. One indeed notes from the data shown in Table 1 that it results in: $(l_0 - l_{\text{cr}})/l_0 < 10^{-4}$.

Fig. 2 illustrates the F_{oct} vs. u and $k_{oct} = dF_{oct}/du$ vs. u responses of two different micro-scale unit cells, whose geometric and mechanical properties are listed in Table 1. The difference between these two units resides in the bars' length and diameter, which are chosen such that the compression forces in the bars in the pre-stressed, unconstrained state are the same for both units (resulting in the same equilibrium configuration and height) and such that buckling of the bars occurs at different compression rates of the unit. In Table 1, a distinction is made between two categories of cables, *i.e.* "Truncating cables" and "Remaining cable", shown in Fig. 1(b). Each category corresponds to cables that are equivalent with respect to the symmetries of the uncompressed truncated octahedron cell. This distinction is necessary when specifying the pre-strains of the cables, since they are not the same for both categories despite the fact that all cables are identical.

Table 1
Geometric and mechanical properties of two micro-scale octahedral units analyzed in the present study.

Initial height (h_0)	5.407 mm
Cables' diameter	0.056 mm
Cables' Young modulus	5.48 GPa
Remaining cables' pre-strain	0.152%
Truncating cables' pre-strain	0.139%
Bars' Young modulus	120 GPa
Bars' rest length for Unit #1	5.1194 mm
Bars' rest length for Unit #2	5.1196 mm
Bars' diameter for Unit #1	0.03078 mm
Bars' diameter for Unit #2	0.02676 mm

We consider micro-scale units with the aim of forming centimeter-scale chains that can be usefully employed in technical applications [23]. The results illustrated in Fig. 2 show that the analyzed units exhibit a force vs. displacement response characterized by a marked stiffening behavior for small values of u. We observe, indeed, that the slope k_{oct} of the F_{oct} vs. u curve (*i.e.*, the tangent axial stiffness of the octahedron unit) initially assumes a small value (soft-response), and next progressively increases, for growing values of u (Fig. 2(b)). We also note that k_{oct} for $u = 0$ is not zero due to the applied prestress [13]. The stiffening behavior under examination gets gradually weaker for larger values of u. Fig. 2 shows indeed that $k_{oct}(u)$ tends to converge to a plateau branch towards the end of the pre-buckling regime. The buckling of the bars occurs when u assumes a critical value u_{buck}, and we note that it results in $u_{buck} = 0.34\ h_0$ for unit #2 (blue curve) and $u_{buck} = 0.24\ h_0$ for unit #1 (red curve).

3. A tensegrity-like potential for the truncated octahedron

This section is aimed at formulating an analytic expression of the potential of a 'tensegrity-like' spring, which suitably mimics the mechanical response illustrated in the previous section, with reference to the pre-buckling regime. Let h denote the height of the truncated octahedron unit in the current (deformed) configuration, which is given by $h = h_0 - u$, where u is the axial displacement defined as in the previous section (positive downward). It is convenient to introduce the height of the unit that marks the first achievement of a buckling event in the bars, that is, the quantity $h_{buck} = h_0 - u_{buck}$, where u_{buck} is defined as in Section 2. We now introduce a non-linear elastic mechanical model defined by the following potential V

$$V(u) \;=\; \alpha_1\, u^2\, \frac{u+\alpha_2}{u+\alpha_3} \tag{2}$$

where α_1 is a constitutive parameter with dimension of force divided by length (*i.e.*, the dimension of an axial stiffness coefficient), while α_2 and α_3 are constitutive parameters with dimensions of length. By differentiating the potential defined by Eq. (2), we easily obtain the axial force F and the tangent axial stiffness k of the model under consideration, which are given by

$$F(u) = \frac{dV}{du} = -\frac{\alpha_1 u^2(\alpha_2+u)}{(\alpha_3+u)^2} + \frac{2\alpha_1 u(\alpha_2+u)}{\alpha_3+u} + \frac{\alpha_1 u^2}{\alpha_3+u} \tag{3}$$

$$k(u) = \frac{dF}{du} = \frac{2\alpha_1 u^2(\alpha_2+u)}{(\alpha_3+u)^3} - \frac{4\alpha_1 u(\alpha_2+u)}{(\alpha_3+u)^2} + \frac{2\alpha_1(\alpha_2+u)}{\alpha_3+u} - \frac{2\alpha_1 u^2}{(\alpha_3+u)^2} + \frac{4\alpha_1 u}{\alpha_3+u} \tag{4}$$

Let the (initial) tangent stiffness for $u = 0$ be denoted by k_0, which, from Eq. (4), is given by

$$k_0 \;=\; 2\,\frac{\alpha_1\alpha_2}{\alpha_3}. \tag{5}$$

The potential given by Eq. (2) was chosen due to the fact that it is able to mimic the main features of the response exhibited by an octahedron tensegrity unit, namely an elastically-stiffening behavior that gets gradually weaker for large values of u. It is worth observing that $k_{oct}(u)$ tends to converge to a positive value at the end of the pre-buckling regime, and that, similarly, $k(u)$ given by Eq. (4) tends to an horizontal asymptote $k = k_f$ for $u \to \infty$, with k_f given by

$$k_f \;=\; 2\,\alpha_1 \;=\; \frac{\alpha_3}{\alpha_2}\,k_0 \tag{6}$$

The use of alternative potentials that are able to effectively capture the response of truncated tensegrity octahedrons is addressed to future work.

We will hereafter assume $k_0 > 0$, as in the case of the prestressed octahedron units analyzed in the previous section, and $k_f > k_0$, in order to model a stiffening-type behavior. Eqs. (5) and (6) point out that such assumptions are matched when $\alpha_1 > 0$, $\alpha_2 > 0$, and $0 < \alpha_2/\alpha_3 < 1$. In particular, a weakly stiffening response is modeled when the α_3/α_2 ratio tends to 1. Figs. 3 graphically illustrate the V vs. u, F vs. u and k vs. u laws, which are obtained using Eqs. (2)–(4) for selected values of the constitutive parameters α_1, α_2 and α_3.

We now introduce the dimensionless kinematic variable $\xi = u/u_{buck}$, and we rewrite the potential (2) as follows

$$\hat{V}(\xi) \;=\; V(u(\xi)) \;=\; \hat{\alpha}_1\,\xi^2\,\frac{\xi+\hat{\alpha}_2}{\xi+\hat{\alpha}_3}. \tag{7}$$

where

$$\hat{\alpha}_1 \;=\; \alpha_1\,u_{buck}^2, \quad \hat{\alpha}_2 \;=\; \frac{\alpha_2}{u_{buck}}, \quad \hat{\alpha}_3 \;=\; \frac{\alpha_3}{u_{buck}} \tag{8}$$

It can be seen that the potential (7) well captures the main feature of the response in compression of the truncated octahedron unit #1 analyzed in the previous section, that is, a stiffening response for small values of u that progressively tends to a linear response as u increases. Fig. 4 illustrate comparisons between the mechanical response of the octahedron unit #1 and the 'tensegrity-like' response governed by the potential (7), for best-fit values of the constitutive parameters. We employed a set of 69 fitting points uniformly spaced along the u-axis for $u \in [0, 0.34h]$, and we used the Mathematica function 'FindFit' with the F_{oct} data to obtain the following best fit parameters: $\alpha_1 = 3181.65$ N/m, $\alpha_2 = 9.0609 \times 10^{-8}$ m and $\alpha_3 = 1.4061 \times 10^{-3}$ m. The results in Fig. 4 show a rather good qualitative matching between the tensegrity-like response and that of the examined octahedron unit, up to $u = u_{buck}$. One observes, in particular, that both such responses describe a stiffening-type behavior progressively turning into a linear response. For the unit #2 analyzed in Section 2, we obtained the fitting parameters $\alpha_1 = 2779.06$ N/m, $\alpha_2 = 1.6015 \times 10^{-4}$ m and $\alpha_3 = 1.5018 \times 10^{-3}$ m. A comparative plot between the mechanical response of unit #2 and the fitted 'tensegrity-like' is not shown here for brevity. The modeling of the buckling- and post-buckling behaviors of octahedron units is beyond the scope of the present study.

4. Wave propagation problem

4.1. Quasi-continuum limit of the equations of motion

The present section is devoted to the computation of the *quasi-continuum* limit of a tensegrity-like mass–spring chain loaded in the dynamic regime. We analyze a chain composed of infinitely many units and we let u_{i-1}, u_i and u_{i+1} denote the displacements exhibited by the masses $i-1$, i and $i+1$, respectively. The equation of motion of the i-the mass in the longitudinal direction is written as follows

$$m\ddot{u}_i = V_u\left(u_{i-1}-u_i\right) - V_u\left(u_i-u_{i+1}\right) \tag{9}$$

By introducing a longitudinal coordinate x along the axis of the chain, we begin by writing the displacement of the ith mass as the realization of a continuous function $u(x,t)$ in correspondence to the current time t and the position x_i of such a mass in the configuration at time zero (*i.e.*, $u_i = u(x,t)$). By using a discrete-to-continuum approach similar to those presented in [27–29], we next employ fourth-order Taylor series expansions for $V_u\left(u_{i-1}-u_i\right)$ and $V_u\left(u_i-u_{i+1}\right)$ in

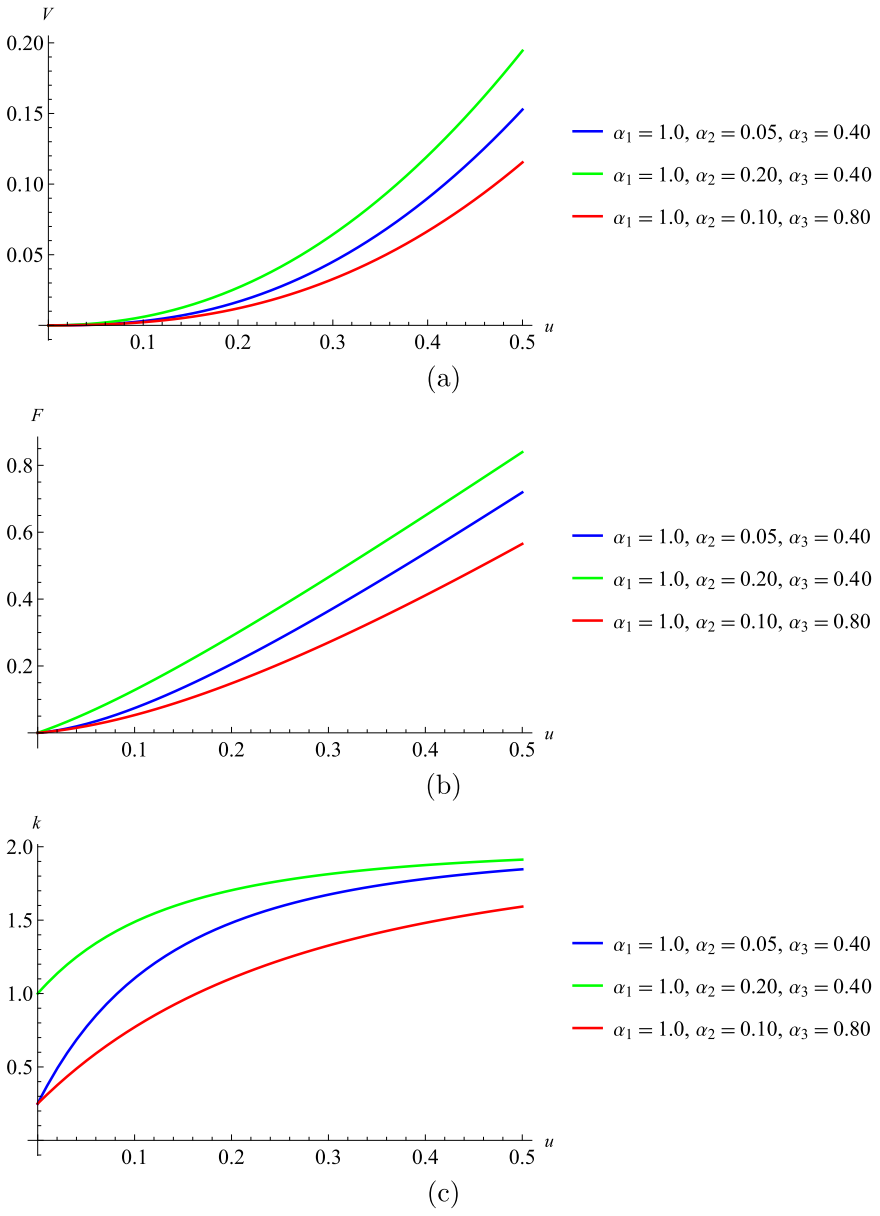

Fig. 3. V vs. u (a), F vs. u (b) and k vs. u (b) for selected values of the constitutive parameters α_1, α_2 and α_3.

Eq. (9). After standard manipulations, we finally get to the following Boussinesq equation [27]

$$u_{tt} = \frac{{h_0}^2}{m}\left[V_u\right]_{xx} + \gamma u_{xxxx} \tag{10}$$

where we have set

$$\gamma = \frac{{h_0}^4\,(k^*)}{12\,m}. \tag{11}$$

with k^* corresponding to the stiffness the unit cell presents on the wave peak. It is useful to introduce the following modified potential, which is a function of the dimensionless variable ξ introduced in the previous section

$$\tilde{V}(\xi) \;=\; \frac{\hat{V}(\xi){h_0}^2}{(m u_{buck}^2)} \;=\; \tilde{\alpha}_1\,\xi^2\,\frac{\tilde{\alpha}_2+\xi}{\tilde{\alpha}_3+\xi}, \tag{12}$$

with

$$\tilde{\alpha}_1 = \frac{\hat{\alpha}_1{h_0}^2}{m u_{buck}^2} = \frac{\alpha_1{h_0}^2}{m}; \quad \tilde{\alpha}_2 = \hat{\alpha}_2; \quad \tilde{\alpha}_3 = \hat{\alpha}_3 \tag{13}$$

By writing Eq. (10) in function of ξ and making use of Eq. (12), we obtain the differential equation

$$\xi_{tt} = \left[\tilde{V}_\xi\right]_{xx} + \gamma\xi_{xxxx} \tag{14}$$

Let us now consider a ξ-wave traveling with speed v, with $\xi \geq 0$ (compression wave). By writing the traveling pulse as $\xi = \phi(x - vt)$, where ϕ is a nonnegative scalar function to be determined, and setting $z = x - vt$, we rewrite Eq. (14) as follows:

$$v^2\phi'' = \left[\tilde{V}_\phi\right]'' + \gamma\phi'''', \tag{15}$$

having used the prime notation for the differentiation with respect to z. A double integration of this equation with respect to z, and the use of asymptotic boundary conditions to eliminate the integration constants, leads us to transform Eq. (15) into the following form

$$\gamma\phi'' = v^2\phi - \left[\tilde{V}_\phi\right]. \tag{16}$$

This equation is identical to Eq.(3.5) obtained in [6] for a different, tensegrity-like mass–spring chain. Multiplying both sides of Eq. (16)

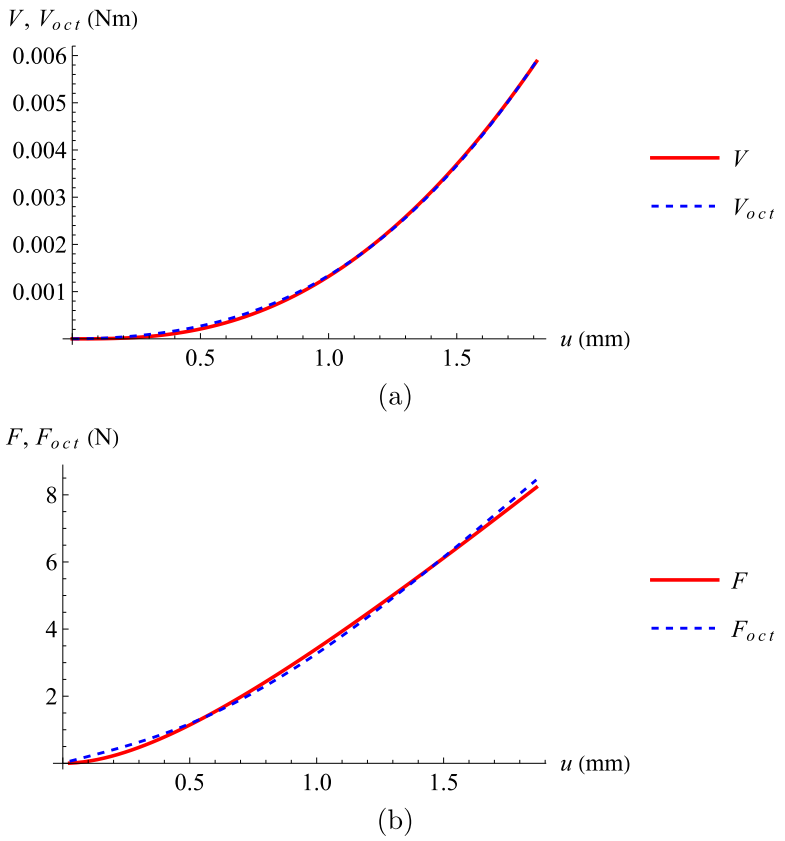

Fig. 4. Fitting of the V_{oct} vs. u (a) and F_{oct} vs. u (b) tensegrity curves (blue-dashed curves) with the analogous tensegrity-like responses V vs. u and F vs. u (red-solid curves). (For interpretation of the references to color in this figure legend, the reader is referred to the web version of this article.)

by ϕ' and performing another integration with respect to z, we obtain

$$\mathcal{F} = v^2\phi^2 - 2\tilde{V} + C, \tag{17}$$

where C is an integration constant, and we have set

$$\mathcal{F} = \gamma\ \phi'^2. \tag{18}$$

Since γ is a positive quantity (see Eq. (11), and due to the assumptions introduced in the previous section, it is worth nothing that it results in $\mathcal{F} \geq 0$ for any ϕ.

4.2. Existence and properties of solitary waves

We here follow the approach presented in [6] to develop a Weierstrass discussion of the solutions of Eq. (17). The drop boundary condition $C = 0$ is introduced into Eq. (17), in order to ensure that the energy disturbance generated by the wave propagation vanishes at a point infinitely distant from the core of the pulse. Using such an assumption and Eq. (12), we deduce from Eq. (17), the following result

$$\mathcal{F} = \phi^2\left[v^2 - 2\ \tilde{\alpha}_1\frac{\tilde{\alpha}_2 + \phi}{\tilde{\alpha}_3 + \phi}\right]. \tag{19}$$

According to Weierstrass's theory, the existence of solitary pulses is related to the existence of two asymptotic points surrounding an inversion point of ϕ [30,31]. One observes that $\phi' = 0$ at such points, implying that they are zero points of $\mathcal{F}$. By inspecting Eq. (19), we note that the points where $\phi = 0$ are zero points of order two for $\mathcal{F}$, which means that they are asymptotic points of the wave profile (cf. Eq. (18)). Let now ϕ approach zero. It can be seen from Eq. (19) that $\mathcal{F} \geq 0$ at this limit condition if and only if the wave speed v is greater than the minimum value

$$v_{min} = \sqrt{2\tilde{\alpha}_1\frac{\tilde{\alpha}_2}{\tilde{\alpha}_3}} = c_0, \tag{20}$$

where $c_0 = h_0\sqrt{\frac{k_0}{m}}$ denotes the speed of sound of the linearized system in the long wavelength limit [32]. For $v = v_{min}$ the continuous system responds in the linear regime and the mechanical waves propagate with the speed of sound. An inversion point (coinciding with the wave peak) is instead found for $\phi = \phi^* \in]0, 1]$, where

$$\phi^* = \frac{\tilde{\alpha}_3 v^2 - 2\tilde{\alpha}_1\tilde{\alpha}_2}{2\tilde{\alpha}_1 - v^2}. \tag{21}$$

One indeed observes from (19) that such a point is a zero of order one for $\mathcal{F}$. With the value of the wave peak, one can now find the value of k^* on Eq. (11), by setting $k^* = k(u_{buck}\ \phi^*)$ on Eq. (4).

By setting $\phi = \phi^* = 1$ into Eq. (21), we obtain the following maximum value v_{max} of the wave speed that guarantees the formation of the solitary pulse:

$$v_{max} = \sqrt{2\tilde{\alpha}_1\frac{1 + \tilde{\alpha}_2}{1 + \tilde{\alpha}_3}}. \tag{22}$$

Since by definition, $\xi = 1$ for $v = v_{max}$, we conclude that the bars of the chain reach a buckling condition when the system is crossed by a solitary wave traveling with such a speed, justifying the name of maximum velocity that we have given to the quantity defined by Eq. (22). Eqs. (20) and (22) highlight that the inequality $\tilde{\alpha}_2 < \tilde{\alpha}_3$ must be satisfied in order to have $v_{min} < v_{max}$. We observe that this inequality is a consequence of the positiveness of α_3 and of the assumption $0 < \alpha_2/\alpha_3 < 1$ of Section 3 (which also implies $0 < \tilde{\alpha_2}/\tilde{\alpha_3} < 1$, cf. Eqs. (8)–(13)) that was made to model a hardening-type response of the tensegrity-like chain.

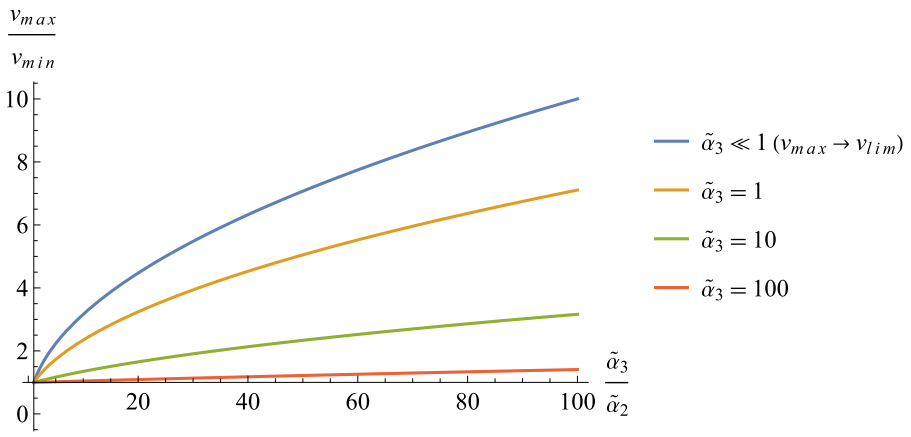

Fig. 5. Ratio between maximum and minimum wave propagation speeds as a function of $\tilde{\alpha}_3/\tilde{\alpha}_2$ for different values of $\tilde{\alpha}_3$.

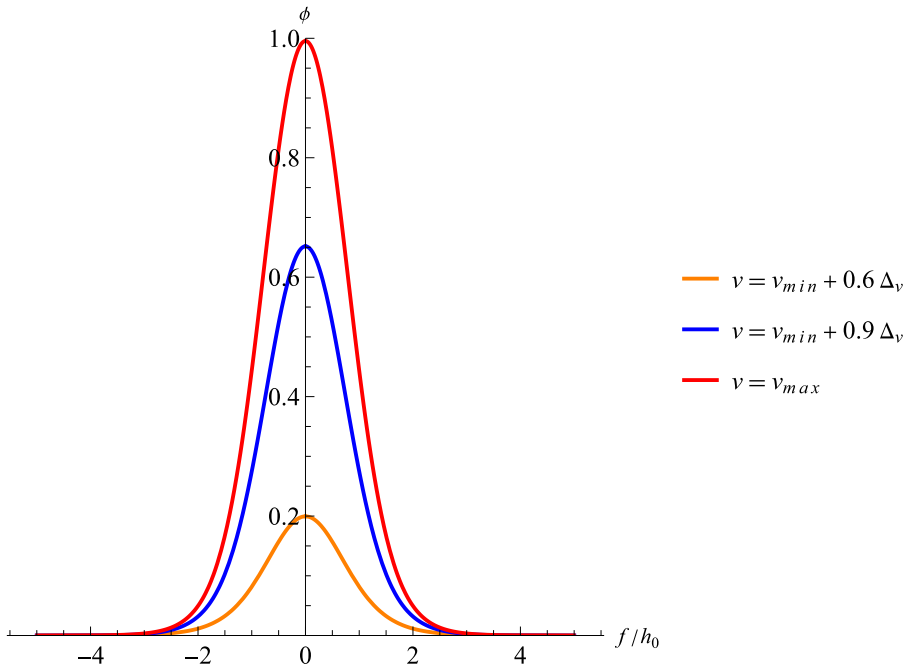

Fig. 6. Solitary pulse profiles computed for different wave speeds and the properties of unit #1.

Fig. 5 illustrates the variation of the quantity v_{max}/v_{min} with the ratio $\tilde{\alpha}_3/\tilde{\alpha}_2$, in correspondence to different values of $\tilde{\alpha}_3$. We observe that v_{min} tends to reach v_{max} when $\tilde{\alpha}_3/\tilde{\alpha}_2$ tends to 1 (for any examined value of $\tilde{\alpha}_3$), as we already observed. On the other hand, the plots in Fig. 5 show that the quantity v_{max}/v_{min} increases as $\tilde{\alpha}_3$ decreases, for any given value of $\tilde{\alpha}_3/\tilde{\alpha}_2$. The absolute maximum value of v_{max} is reached when $\tilde{\alpha}_2 < \tilde{\alpha}_3 \ll 1$, *i.e.*, when u_{buck} tends to infinity (no bars buckling, cf. Eqs. (8)–(13))). We let v_{lim} denote such a limit value of v_{max}, which is given by

$$v_{lim} = \sqrt{2\tilde{\alpha}_1} \tag{23}$$

implying

$$\frac{v_{lim}}{v_{min}} = \sqrt{\frac{\tilde{\alpha}_3}{\tilde{\alpha}_2}} = \sqrt{\frac{k_f}{k_0}}. \tag{24}$$

We now move on to determine the shape of the solitary pulse, by introducing the inverse function $f = \pm z$. Since Eq. (18) implies $\frac{d\phi}{dz} = \sqrt{\frac{F}{\gamma}}$, one can write

$$f := \int \sqrt{\frac{\gamma}{F}}\, d\phi = \pm z \tag{25}$$

that results in

$$f = 2\sqrt{\gamma}\ \frac{\psi \tan^{-1}\left(\frac{\chi}{\rho}\right) - \rho \tan^{-1}\left(\frac{\chi}{\psi}\right)}{\psi\rho} \tag{26}$$

where

$$\chi = \sqrt{v^2 - 2\tilde{\alpha}_1\ \frac{\phi + \tilde{\alpha}_2}{\phi + \tilde{\alpha}_3}}, \qquad \rho = \sqrt{{c_0}^2 - v^2}, \qquad \psi = \sqrt{{v_{lim}}^2 - v^2} \tag{27}$$

Once one obtains the plot of the function $f(\phi)$, through Eq. (26), one can switch the axes of this graph in order to obtain the plot of the shape of the pulse $\phi(f)$. Fig. 6 illustrates the pulse profiles that have been obtained through such a procedure, considering different wave speeds ranging between $v_{min} = 0.077422$ m/s and $v_{max} = 7.2601$ m/s, with the fitted potential of unit # 1 and $m = 2$ g. In this plot, we set $\Delta_v = v_{max} - v_{min}$ and we scaled f by dividing such quantity by the initial height of the unit h_0 (in the discrete system). The dimensionless quantity f/h_0 gives the number of lattice spaces embraced by the solitary pulse, when passing to the continuum limit. We observe from Fig. 6 that the wave

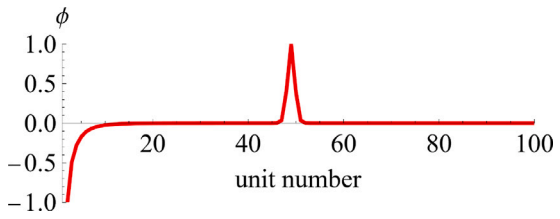

Fig. 7. Longitudinal displacement along the chain with 100 units for $v = v_{max}$, using the F_{ntl} model.

width does not change significantly in correspondence to the examined values of the wave speed, while the height of the ξ-pulse varies from zero to one. Such a result significantly differs from those presented in Ref. [6], where instead a strong localization behavior of the strain pulses was observed for increasing values of the wave speed.

5. Numerical simulations

The present section is aimed at validating the theoretical results of Section 4 via numerical simulations of the wave dynamics of two different chains made of tensegrity-like units. All units in a chain are modeled as identical nonlinear, one-dimensional springs, and identical masses are placed between each pair of adjacent springs and at both ends of the chain. The difference between the two types of studied chains resides in the nonlinear force function of the springs used during simulations. Hereafter, we use the label F_{ntl} to refer to the numerical implementation of the tensegrity-like model, which makes use of the fitting parameters α_1, α_2 and α_3 listed in Section 3 for unit #1, and we employ the label F_{oct} to denote the mechanical model of the truncated tensegrity octahedron introduced in Section 2. Finally, we label the analytic formulation of the tensegrity-like model defined by Eq. (3) with the symbol F.

The examined chains are composed of n masses and $n-1$ units, and exhibit a mass $m = 2$ g. The equations of motions of the resulting n-dimensional system, obtained by substituting the appropriate force function in Eq. (2), is written

$$\ddot{U} = \frac{1}{m}\boldsymbol{F}(U), \tag{28}$$

where U is the vector of displacements of the chain's masses, and $\boldsymbol{F}(U)$ the vector of forces applied at these masses. The chain is therefore modeled as a second-order system of mass and springs in series.

At $t = 0$, the springs' displacements and the initial velocities of the masses are set to zero, except for the first mass, which is given a positive velocity to initiate the wave propagation. For $t > 0$, the state of the system is determined by solving the ODE Eq. (28) via the *Matlab* function 'ode45', which is based on the Dormand–Prince pair, an explicit fifth-order Runge–Kutta method [33,34]. This method uses an adaptive time step, which we bounded from above by $\frac{1}{100}\frac{k(0)}{m}$ via the function's options, where $k(0)$ is the stiffness of the considered nonlinear spring at zero displacement.

We report the results obtained with both nonlinear springs types for a chain with $n = 100$ and compare them to the theoretical predictions from the analytical tensegrity-like potential. We first show in Fig. 7 the behavior of the longitudinal displacement through the 100 units when a pulse is passing through the 49th spring. This Figure was obtained using the F_{ntl} model and $v = v_{max}$. In Fig. 8(a,b), one can see two solitary waves found in the domain $\phi \in]0, 1]$ with the F_{ntl} model. The pulses are represented on the instants they pass through the 49th and 51st

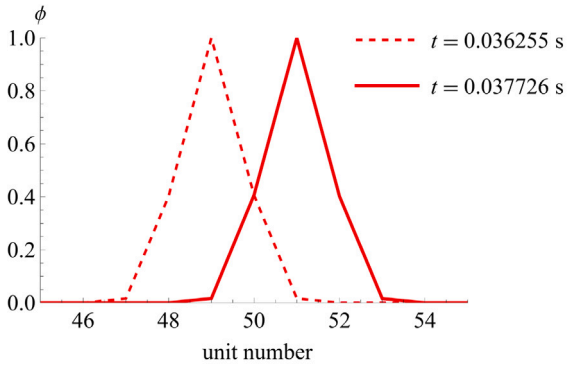

(a) F_{ntl}: $v = 7.3532$ m/s and $\phi^* = 1$

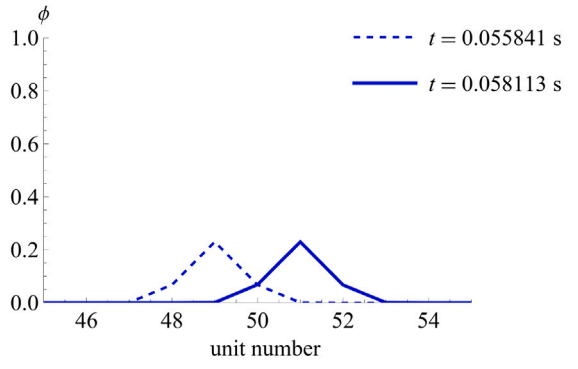

(b) F_{ntl}: $v = 4.7596$ m/s and $\phi^* = 0.23$

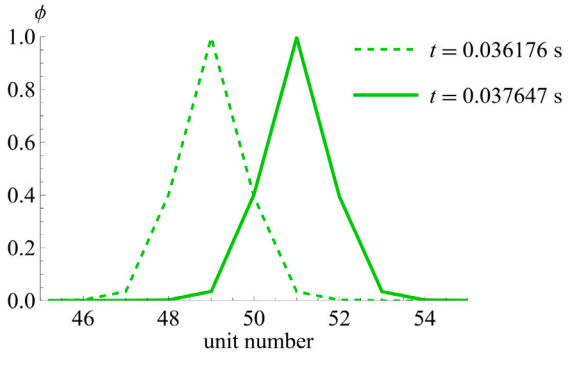

(c) F_{oct}: $v = 7.3532$ m/s and $\phi^* = 1$

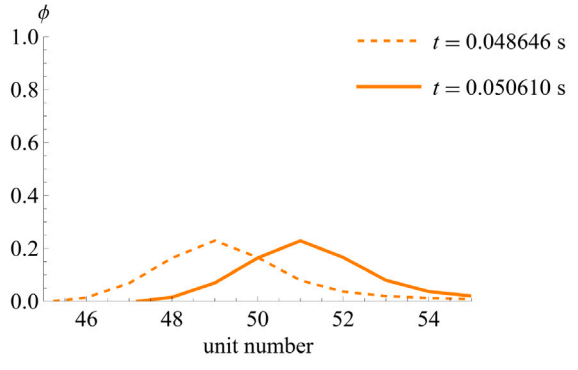

(d) F_{oct}: $v = 5.5067$ m/s and $\phi^* = 0.23$

Fig. 8. Numerical solitary waves determined with the F_{ntl} (a,b) and F_{oct} (c,d) models passing through the 49th and 51st springs.

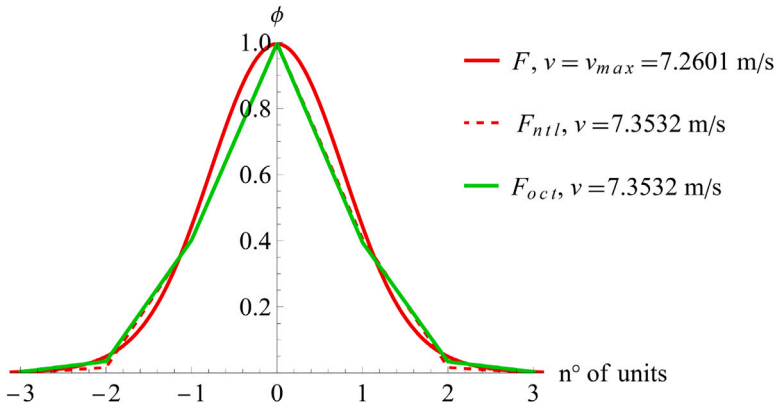

(a) $\phi^* = 1$

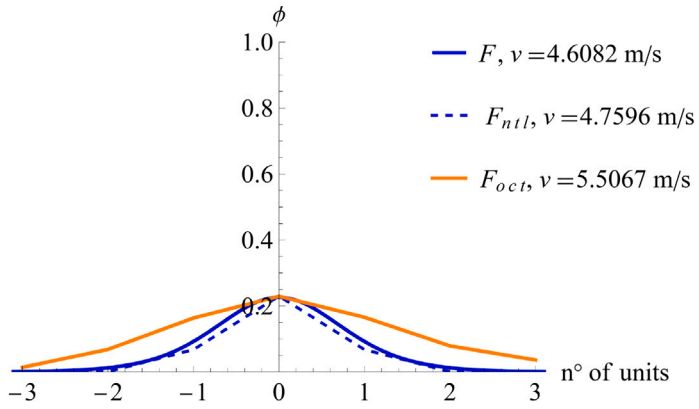

(b) $\phi^* = 0.23$

Fig. 9. Analytical (F) and numerical (F_{ntl}, F_{oct}) pulses for $\phi^* = 1$ (a) and $\phi^* = 0.23$ (b).

springs, defined as the respective times for which the displacements of these springs are maximized. Their speeds are found by dividing $2h_0$ by the time that it takes for the wave to travel from the 49th to the 51st springs. In Fig. 8(a), a pulse with $v = 7.3532$ m/s and amplitude $\phi^* = 1$ is represented at the times $t = 0.036255$ and $t = 0.037726$. In Fig. 8(b), a pulse with $v = 4.7596$ m/s and amplitude $\phi^* = 0.23$ is represented at the times $t = 0.055841$ and $t = 0.058113$. By using the numerical values of $\phi^* = 1$ and $\phi^* = 0.23$ in Eq. (21), one can find the values $v = v_{max} = 7.2601$ m/s and $v = 4.6082$ m/s, respectively, showing a good match of the relation between the wave speed and wave amplitude found numerically and analytically with the adopted tensegrity-like potential. It is also important to point out that the minimum speed found by the numerical simulations with the F_{ntl} model was equal to 0.073321 m/s = 0.95 v_{min} (Eq. (20)). Moreover, when the domain of u was not restricted until the buckling point, it was possible to find wave solutions with $\phi^* > 1$ with speeds up to 9.1641 m/s that corresponds to 97% of the ideal maximum $v_{lim} = 9.6446$ m/s (Eq. (23)), also validating the analytical speed range.

By using a similar approach, we determined the wave speeds obtained with the F_{oct} model, with their results being shown in Figs. 8(c) and 8(d). For $\phi^* = 1$, we found $v = 7.3532$ m/s, which corresponds to an error that is smaller than 0.01% compared with the numerical speed obtained with F_{ntl}. For $\phi^* = 0.23$, the computed wave speed is $v = 5.5067$ m/s, which results in an error of approximately 16% compared with the wave speeds found previously for $\phi^* = 0.23$. This shows that adopting the tensegrity-like potential only results in a modest loss of accuracy concerning the determination of the wave speeds, especially for higher values of ϕ^*. The loss of accuracy for smaller values of ϕ^* is explained by the fact that the tensegrity-like model better fits the force and potential laws of the real tensegrity unit for large values of u (see Fig. 4). We address an improvement of the fitting procedure presented in this work, which employs two different fitting models for small and large values of u, to future work.

Fig. 9 shows a comparison between the numerical pulses obtained with F_{oct} and F_{ntl} represented in Fig. 8, and their analytical correspondents for the same ϕ^*. For F_{ntl}, the pulse width does not vary significantly for the different wave speeds, as observed analytically in Section 4. For $\phi^* = 1$, one can notice a good match between the results when overlapping the pulses found with the three models. For $\phi^* = 0.23$, there is a very good match between the analytical pulse and the numerical F_{ntl}. When using the F_{oct} model, the solitary wave affects more units for $\phi^* = 0.23$, resulting in a wider pulse. These results suggest that although the proposed tensegrity-like model gives good results when analyzing the propagation of solitary waves in truncated octahedron tensegrity chains, it presents a higher accuracy when considering higher values of ϕ^*.

6. Concluding remarks

This work investigated the existence and the properties of compression solitary waves propagating through one-dimensional tensegrity-like mass–spring chains, whose units exhibit a mechanical response

similar to that exhibited by truncated octahedrons [13,14,16,17]. Such a response features an initially soft-response followed by a hardening behavior that ends with a linear branch, in correspondence to the pre-buckling regime. The existence of compression solitary waves was demonstrated analytically by using Weierstrass's theory of one-dimensional Lagrangian systems, and a suitable range of wave speeds has been shown to support the propagation of compression solitary waves.

An analytical law for the shape of the pulses has been derived in implicit form. Numerical simulations using the tensegrity-like model and the real force vs. displacement response of the analyzed chains highlighted the accuracy of the analytic results and provided their validation. The tensegrity-like numerical simulations indeed confirmed the validity of the analytic results found for the wave speed ranges that support solitary waves, and the shape of the propagating pulses. A very good matching was observed between the simulations corresponding to the true tensegrity force vs. displacement response and the tensegrity-like model, in the case of pulses featuring high amplitudes.

We address an analytical study on the post-buckling behavior of the tensegrity octahedron to future work. Additional lines of future research include an extension of the Weierstrass's approach presented in this work to two- and three-dimensional metamaterials equipped with a variety of tensegrity units with non-linear response [35–37], as well as studies on the stability properties of solitary waves propagating through tensegrity mass–spring lattices [38,39].

CRediT authorship contribution statement

Julia de Castro Motta: Writing – review & editing, Writing – original draft, Investigation, Funding acquisition, Formal analysis, Conceptualization. **Kevin Garanger:** Writing – review & editing, Writing – original draft, Validation, Software, Investigation, Data curation, Conceptualization. **Julian J. Rimoli:** Writing – review & editing, Writing – original draft, Supervision, Project administration, Methodology, Formal analysis, Conceptualization.

Declaration of competing interest

The authors declare that they have no known competing financial interests or personal relationships that could have appeared to influence the work reported in this paper.

Data availability

Data will be made available on request.

Acknowledgments

The authors gratefully acknowledge the great support received by Fernando Fraternali, Ada Amendola (University of Salerno) and Giuseppe Saccomandi (University of Perugia) in the development of the numerical and analytical results presented in this work.

Funding

Julia de Castro Motta was supported by Italian Ministry of Foreign Affairs and International Cooperation within the Italy-USA Science and Technology Cooperation Program 2023–2025, Project "Next-generation green structures for natural disaster-proof buildings", grant number US23GR15.

References

[1] R.E. Skelton, M.C. De Oliveira, Tensegrity Systems, vol. 1, Springer, 2009, http://dx.doi.org/10.1007/978-0-387-74242-7.
[2] M.-H. Lu, L. Feng, Y.-F. Chen, Phononic crystals and acoustic metamaterials, Mater. Today 12 (12) (2009) 34–42, http://dx.doi.org/10.1016/S1369-7021(09)70315-3.
[3] K. Bertoldi, V. Vitelli, J. Christensen, M. Van Hecke, Flexible mechanical metamaterials, Nat. Rev. Mater. 2 (11) (2017) 1–11, http://dx.doi.org/10.1038/natrevmats.2017.66.
[4] M. Kadic, G.W. Milton, M. van Hecke, M. Wegener, 3D metamaterials, Nat. Rev. Phys. 1 (3) (2019) 198–210, http://dx.doi.org/10.1038/s42254-018-0018-y.
[5] M.I. Hussein, M.J. Leamy, M. Ruzzene, Dynamics of phononic materials and structures: Historical origins, recent progress, and future outlook, Appl. Mech. Rev. 66 (4) (2014) 040802, http://dx.doi.org/10.1115/1.4026911.
[6] A. Amendola, An analytic study on the properties of solitary waves traveling on tensegrity-like lattices, Int. J. Non-Linear Mech. 148 (2023) 104264, http://dx.doi.org/10.1016/j.ijnonlinmec.2022.104264.
[7] F. Fraternali, G. Carpentieri, A. Amendola, R.E. Skelton, V.F. Nesterenko, Multiscale tunability of solitary wave dynamics in tensegrity metamaterials, Appl. Phys. Lett. 105 (20) (2014) http://dx.doi.org/10.1063/1.4902071.
[8] F. Fraternali, L. Senatore, C. Daraio, Solitary waves on tensegrity lattices, J. Mech. Phys. Solids 60 (6) (2012) 1137–1144, http://dx.doi.org/10.1016/j.jmps.2012.02.007.
[9] A. Micheletti, G. Ruscica, F. Fraternali, On the compact wave dynamics of tensegrity beams in multiple dimensions, Nonlinear Dynam. 98 (4) (2019) 2737–2753, http://dx.doi.org/10.1007/s11071-019-04986-8.
[10] R.K. Pal, M. Ruzzene, J.J. Rimoli, Tunable wave propagation by varying prestrain in tensegrity-based periodic media, Extreme Mech. Lett. 22 (2018) 149–156, http://dx.doi.org/10.1016/j.eml.2018.06.005.
[11] K. Liu, T. Zegard, P.P. Pratapa, G.H. Paulino, Unraveling tensegrity tessellations for metamaterials with tunable stiffness and bandgaps, J. Mech. Phys. Solids 131 (2019) 147–166, http://dx.doi.org/10.1016/j.jmps.2019.05.006.
[12] D. De Tommasi, G. Puglisi, F. Trentadue, Tunable shear stiffness in a metamaterial sheet, Meccanica 54 (2019) 2029–2037, http://dx.doi.org/10.1007/s11012-019-00994-5.
[13] J.J. Rimoli, R.K. Pal, Mechanical response of 3-dimensional tensegrity lattices, Composites B 115 (2017) 30–42, http://dx.doi.org/10.1016/j.compositesb.2016.10.046.
[14] J.J. Rimoli, A reduced-order model for the dynamic and post-buckling behavior of tensegrity structures, Mech. Mater. 116 (2018) 146–157, http://dx.doi.org/10.1115/1.4039427.
[15] J. Bauer, J.A. Kraus, C. Crook, J.J. Rimoli, L. Valdevit, Tensegrity metamaterials: Toward failure-resistant engineering systems through delocalized deformation, Adv. Mater. 33 (10) (2021) 2005647, http://dx.doi.org/10.1002/adma.202005647.
[16] J.J. Rimoli, On the impact tolerance of tensegrity-based planetary landers, in: 57th AIAA/ASCE/AHS/ASC Structures, Structural Dynamics, and Materials Conference, 2016, p. 1511, http://dx.doi.org/10.2514/6.2016-1511.
[17] K. Garanger, I. del Valle, M. Rath, M. Krajewski, U. Raheja, M. Pavone, J.J. Rimoli, Soft tensegrity systems for planetary landing and exploration, in: Earth and Space 2021, 2021, pp. 841–854, http://dx.doi.org/10.1061/9780784483374.078.
[18] J. Zhang, M. Ohsaki, J.J. Rimoli, K. Kogiso, Optimization for energy absorption of 3-dimensional tensegrity lattice with truncated octahedral units, Compos. Struct. 267 (2021) http://dx.doi.org/10.1016/j.compstruct.2021.113903.
[19] V.F. Nesterenko, Propagation of nonlinear compression pulses in granular media, J. Appl. Mech. Tech. Phys.(Engl. Transl.);(United States) 24 (5) (1984) http://dx.doi.org/10.1007/BF00905892.
[20] V.F. Nesterenko, Dynamics of Heterogeneous Materials, Springer Science & Business Media, 2013.
[21] C. Daraio, D. Ngo, V.F. Nesterenko, F. Fraternali, Highly nonlinear pulse splitting and recombination in a two-dimensional granular network, Phys. Rev. E 82 (3) (2010) 036603, http://dx.doi.org/10.1103/PhysRevE.82.036603.
[22] C. Daraio, V.F. Nesterenko, E.B. Herbold, S. Jin, Tunability of solitary wave properties in one-dimensional strongly nonlinear phononic crystals, Phys. Rev. E 73 (2006) 026610, http://dx.doi.org/10.1103/PhysRevE.73.026610.
[23] A. Spadoni, C. Daraio, Generation and control of sound bullets with a nonlinear acoustic lens, Proc. Natl. Acad. Sci. 107 (16) (2010) 7230–7234, http://dx.doi.org/10.1073/pnas.1001514107.
[24] C.M. Donahue, P.W. Anzel, L. Bonanomi, T.A. Keller, C. Daraio, Experimental realization of a nonlinear acoustic lens with a tunable focus, Appl. Phys. Lett. 104 (1) (2014) http://dx.doi.org/10.1063/1.4857635.
[25] Z. Chen, W. Zhou, C. Lim, Active control for acoustic wave propagation in nonlinear diatomic acoustic metamaterials, Int. J. Non-Linear Mech. 125 (2020) 103535, http://dx.doi.org/10.1016/j.ijnonlinmec.2020.103535.
[26] E. Polak, G. Ribière, Note sur la convergence de méthodes de directions conjuguées, Rev. Française d'informatique et de Recherche Opérationnelle. Sér. Rouge 3 (R1) (1969) 35–43, http://dx.doi.org/10.1051/m2an/196903R100351.

[27] P. Rosenau, Dynamics of nonlinear mass-spring chains near the continuum limit, Phys. Lett. A 118 (5) (1986) 222–227, http://dx.doi.org/10.1016/0375-9601(86)90402-8.
[28] P.J. Olver, A. Stern, Dispersive fractalisation in linear and nonlinear Fermi-Pasta-Ulam-Tsingou lattices, European J. Appl. Math. 32 (5) (2021) 820–845, http://dx.doi.org/10.1017/S095679252000042X.
[29] P. Rosenau, Dynamics of dense lattices, Phys. Rev. B 36 (11) (1987) 5868, http://dx.doi.org/10.1103/PhysRevB.36.5868.
[30] M. Destrade, G. Gaeta, G. Saccomandi, Weierstrass's criterion and compact solitary waves, Phys. Rev. E 75 (4) (2007) 047601, http://dx.doi.org/10.1103/PhysRevE.75.047601.
[31] G. Saccomandi, Elastic rods, Weierstrass' theory and special travelling waves solutions with compact support, Int. J. non-linear Mech. 39 (2) (2004) 331–339, http://dx.doi.org/10.1016/S0020-7462(02)00192-0.
[32] N.W. Ashcroft, N.D. Mermin, Solid State Physics, Holt-Saunders, 1976.
[33] L.F. Shampine, M.W. Reichelt, The matlab ode suite, SIAM J. Sci. Comput. 18 (1) (1997) 1–22, http://dx.doi.org/10.1137/S1064827594276424.
[34] J.R. Dormand, P.J. Prince, A family of embedded Runge-Kutta formulae, J. Comput. Appl. Math. 6 (1) (1980) 19–26, http://dx.doi.org/10.1016/0771-050X(80)90013-3.
[35] D. De Tommasi, G. Puglisi, F. Trentadue, Elastic response of an optimal tensegrity-type metamaterial, Front. Mater. 6 (2019) 24, http://dx.doi.org/10.3389/fmats.2019.00024.
[36] I. Mascolo, A. Amendola, G. Zuccaro, L. Feo, F. Fraternali, On the geometrically nonlinear elastic response of class θ=1 tensegrity prisms, Front. Mater. 5 (2018) 16, http://dx.doi.org/10.3389/fmats.2018.00016.
[37] F. Fraternali, G. Carpentieri, A. Amendola, On the mechanical modeling of the extreme softening/stiffening response of axially loaded tensegrity prisms, J. Mech. Phys. Solids 74 (2015) 136–157, http://dx.doi.org/10.1016/j.jmps.2014.10.010.
[38] J.G. Berryman, Stability of solitary waves in shallow water, Phys. Fluids 19 (6) (1976) 771–777, http://dx.doi.org/10.1063/1.861569.
[39] R.L. Pego, M.I. Weinstein, Convective linear stability of solitary waves for Boussinesq equations, Stud. Appl. Math. 99 (4) (1997) 311–375, http://dx.doi.org/10.1111/1467-9590.00063.